Journal of Magnetic Resonance 242 (2014) 113–125

Contents lists available at ScienceDirect

Journal of Magnetic Resonance

journal homepage: www.elsevier.com/locate/jmr

An ultra-broadband low-frequency magnetic resonance system

S. Mandal [a,*], S. Utsuzawa [a], D.G. Cory [b], M. Hürlimann [a], M. Poitzsch [a], Y.-Q. Song [a]

[a] Schlumberger-Doll Research, Cambridge, MA 02139, USA
[b] University of Waterloo, Waterloo, ON N2L 3G1, Canada

ARTICLE INFO

Article history:
Received 30 October 2013
Revised 10 February 2014
Available online 4 March 2014

Keywords:
Hardware
Broadband
Un-tuned
Low-frequency

ABSTRACT

MR probes commonly employ resonant circuits for efficient RF transmission and low-noise reception. These circuits are narrow-band analog devices that are inflexible for broadband and multi-frequency operation at low Larmor frequencies. We have addressed this issue by developing an ultra-broadband MR probe that operates in the 0.1–3 MHz frequency range without using conventional resonant circuits for either transmission or reception. This "non-resonant" approach significantly simplifies the probe circuit and allows robust operation without probe tuning while retaining efficient power transmission and low-noise reception. We also demonstrate the utility of the technique through a variety of NMR and NQR experiments in this frequency range.

1. Introduction

Magnetic resonance (MR) probes typically use resonant circuits to achieve efficient RF power transmission and low-noise reception around the Larmor frequency $\omega_0 = \gamma B_0$ [1]. These circuits consist of the sample coil (inductance L) that both generates B_1 fields and detects MR signals, and a passive tuning and impedance-matching network. In a single-frequency probe, this network typically consists of a single tuning capacitor (capacitance C) in parallel with the coil, and a second "matching" capacitor in series with it. Such a network acts as an analog filter tuned to a resonance frequency of $\omega_c = 1/\sqrt{LC}$ that only allows efficient power transmission and low-noise reception over a bandwidth of approximately $2\omega_c/Q$. Here Q, the quality factor of the network, is often dominated by that of the coil, i.e. $Q \approx Q_L = \omega_c L/R$ where R is its effective series resistance. Quality factors of 100 or higher are common for non-conducting samples, which makes the operating bandwidth of the probe much smaller than ω_0. Multi-frequency MR probes can be built by combining several resonant circuits within the tuning network, but are complex, expensive, and require frequent tuning. Such multi-frequency probes are particularly challenging at low Larmor frequencies where the probe bandwidth ω_0/Q can become comparable or smaller than the nutation frequency $\omega_1 = \gamma B_1$.

This paper describes a broadband or non-resonant (NR) front-end system for MR experiments at frequencies below 3 MHz that addresses these issues by not using resonant circuits for excitation or reception [2,3]. A broad range of field applications are promising at such low frequencies, such as real-time process monitoring (e.g. food [4]), geological prospecting (e.g. well-logging for petroleum and mining [5,6]), and detection of explosives and other illicit materials using nuclear quadrupole resonance (NQR) [7,8]. Our system uses conventional RF pulses to manipulate the spins, unlike non-resonant methods based on reversing the direction of the static magnetic field [9]. However, unlike in a tuned probe, our transmitter directly controls the RF voltage across the coil, which makes the spin excitation insensitive to changes in coil and sample losses. In addition, our receiver also directly senses the MR voltage induced in the coil, which makes signal reception also insensitive to these losses (which change the coil Q). Similar benefits can be obtained through Cartesian feedback techniques [10], but these are difficult to implement in ultra-broadband systems.

Our approach is fundamentally different from previously reported broadband designs using delay lines or transmission lines [11–14]. Such probes are considerably less sensitive detectors than simple coil geometries, such as solenoids. By contrast, we use a standard, highly sensitive solenoid coil as our detector. The broadband nature of our electronics allows rapid switching of the operating frequency for multi-frequency and multi-nuclear MR experiments without tuning. The final detection bandwidth, which is usually small to maximize the signal-to-noise ratio (SNR), is easily adjustable since it can be set digitally during later signal processing. With this broadband front-end, we have therefore developed a digitally-defined MR system that is conceptually similar to modern RF systems found in mobile devices, which also combine broadband analog front-ends with digital hardware and

---

* Corresponding author.
E-mail addresses: SMandal@slb.com (S. Mandal), SUtsuzawa@slb.com (S. Utsuzawa), dcory@iqc.ca (D.G. Cory), hurlimann@slb.com (M. Hürlimann), poitzsch1@slb.com (M. Poitzsch), ysong@slb.com (Y.-Q. Song).

http://dx.doi.org/10.1016/j.jmr.2014.02.019
1090-7807/

software for narrow-band channel selection. We now describe the key features of our NR design and demonstrate its operation in several multi-frequency experiments. This paper focuses on applications in the 0.1–3 MHz frequency range with moderately-sized sample coils, but it is possible to extend the technique to higher frequencies if smaller coils are used.

2. Non-resonant system

A simplified block diagram of our NR system is shown in Fig. 1. The key features include a single un-tuned transmit and receive coil containing the sample, a switching transmitter using a H-bridge circuit, a transformer-based low-noise, broadband preamplifier, and a switch-based broadband duplexer with isolated driver. A commercial NMR console (Kea 2, Magritek, NZ) is used to program pulse sequences, synthesize low-power RF signals, digitize the receiver output, and perform further signal processing. The system is capable of generating two channels of RF pulses for double resonance experiments.

2.1. Transmitter

Our basic non-resonant transmitter design consists of a set of four MOSFET switches (denoted by A, B, C, and D) arranged in a circuit known as an H-bridge or full bridge, as shown in Fig. 1 [2]. The switches are controlled by two non-overlapping digital signals denoted as ϕ_1 and ϕ_2, as shown in Fig. 2. These signals are created by comparing the low-power sinusoidal waveforms (of amplitude V_{in}) that are generated by the Kea console with two reference voltages V_+ and $V_- = -V_+$. They alternately drive the two sets of switches, AD and BC respectively, such that the high-voltage source V_{BB} is connected with alternating polarity across the coil to create an oscillatory coil current. A load resistor R_1 can be used in series with V_{BB} in order to limit the current into the MOSFETs.

The *duty cycle* of ϕ_1 and ϕ_2 is defined as the fraction of time these waveforms are active (at a logical value of 1) during an RF pulse. It is given by

$$D = \frac{1}{2} - \frac{\sin^{-1}(V_{\pm}/V_{in})}{\pi} \tag{1}$$

Any power MOSFET is also associated with a parallel *body diode* that is intrinsic to the structure of the device. The combined device acts as an active switch (controlled by the gate voltage) for forward currents, which flow from the drain terminal to the source terminal through the MOSFET. It also acts as a passive switch (controlled by the drain-source voltage) for reverse currents, which flow from the source terminal to the drain terminal through the diode.

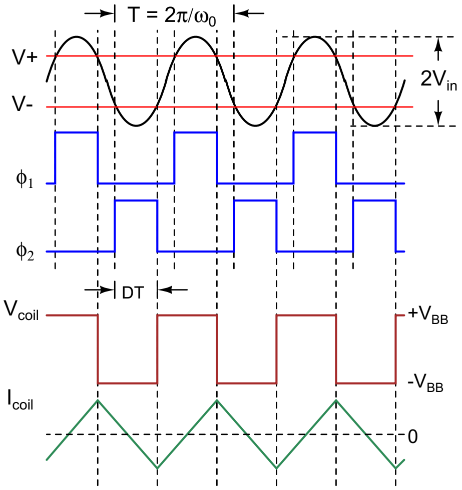

Fig. 2. Important waveforms for the non-resonant transmitter.

The transmitter circuit can operate in two distinct modes. The continuous conduction mode (CCM) is shown in Fig. 2. It occurs when $D \geqslant D_{crit}$, where D_{crit} is known as the critical duty cycle. The discontinuous conduction mode (DCM) occurs when $D < D_{crit}$, and is characterized by a period when the current in the coil is zero.

Fig. 3 shows the four possible states of conduction of the H-bridge circuit (labeled 1–4). The key to understanding these states is to remember that the coil current cannot change suddenly, i.e., must remain continuous. In state 1 current is being carried by two of the body diodes. This state continues till the current reverses direction and the diodes switch off. The two MOS switches controlled by ϕ_1 then start carrying the coil current, resulting in state 2. Once phase ϕ_1 turns off the coil current continues to flow through the two remaining body diodes (state 3) until it reverses direction. At this point it begins to flow through the two MOS switches controlled by phase ϕ_2 (state 4). Eventually the ϕ_2 signal turns off, the circuit returns to state 1 and the cycle continues.

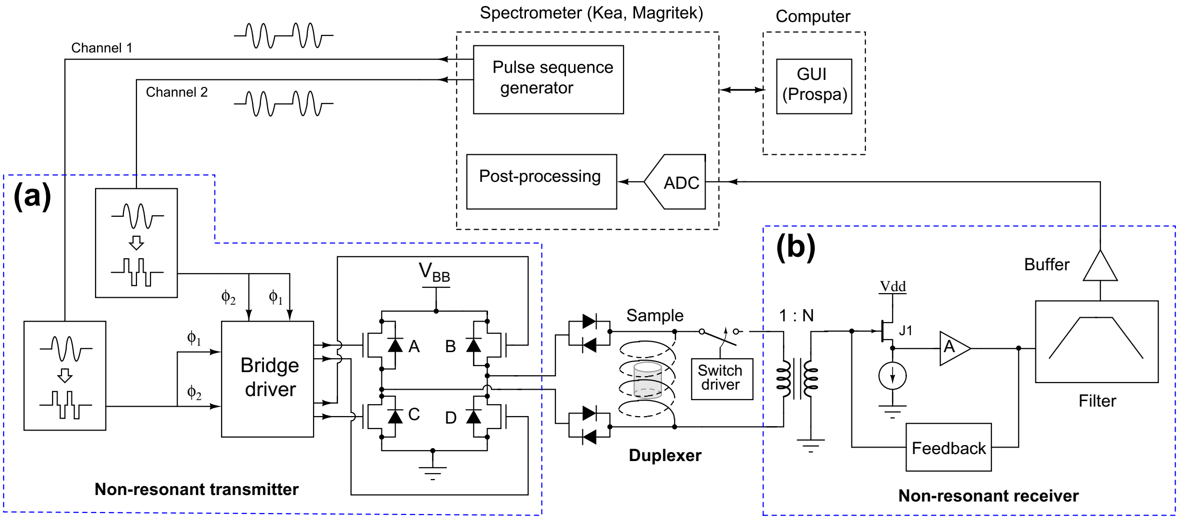

Fig. 1. Block diagram of the non-resonant MR system. (a) Transmitter block: the RF pulses are created by the two signals (ϕ_1 and ϕ_2) that control a H-bridge circuit. (b) Receiver block: the simplified front-end circuit uses a broadband $1:n$ step-up transformer.

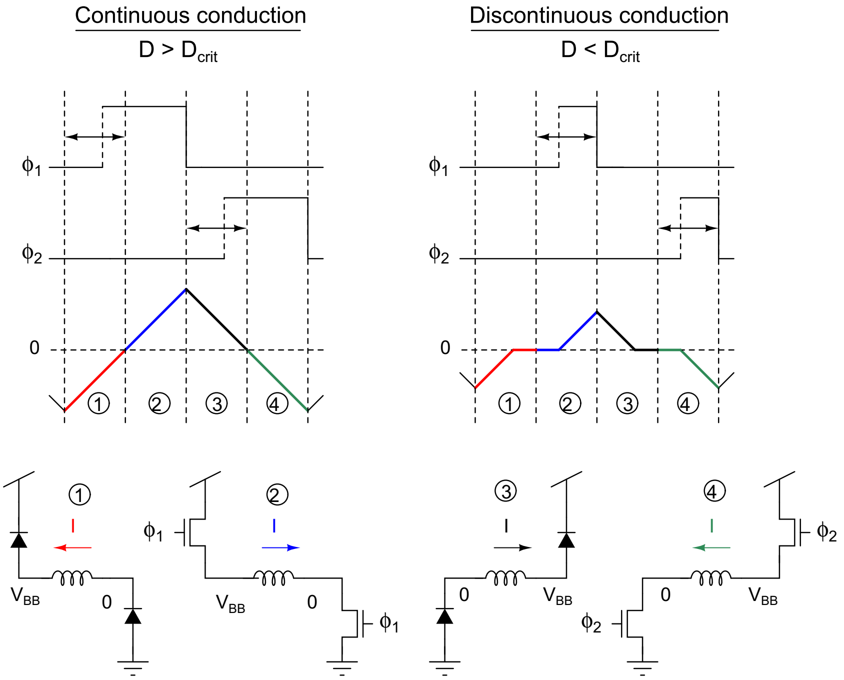

Fig. 3. States of operation of the H-bridge circuit in the continuous (left), and discontinuous (right) conduction modes.

The circuit will be in the CCM if ϕ_1 turns on before the current in the coil reverses direction, i.e., before the transition between states 1 and 2. A similar condition holds for ϕ_2 and the transition between states 3 and 4. Both conditions are satisfied if $D > D_{crit}$. When $D < D_{crit}$ the phases turn on after the coil current reaches zero, and thus there is a period when it remains zero, resulting in the DCM. In the ideal case, i.e., with zero coil and switch resistances and zero diode forward voltage drops, a simple symmetry argument shows that $D_{crit} = 1/4$.

We now analyze the CCM. To first order, we may assume that the switches are ideal, and that there are no stray capacitances. In this case the current through the coil at time t after turning on the switch is given by

$$I_{coil}(t) = \pm\frac{V_{BB}}{R}\left(1 - e^{-t/\tau_1}\right) \tag{2}$$

Here we have assumed $I(0) = 0$ and defined the time constant $\tau_1 = L/R$. The signs correspond to the positive and negative phases, respectively. At Larmor frequencies that are high enough for $t \ll \tau_1$, i.e., when $1/f_0 \ll \tau_1$, the expression above can be linearized to $I = \pm V_{batt}t/L$, independent of R and thus Q. As a result, a symmetric triangular current waveform is produced in the coil. This waveform can be written as the following Fourier series:

$$I_{coil}(t) = \frac{V_{BB}(4/\pi)}{\omega_0 L}\sum_{n=1,3,5,\ldots}^{\infty}\frac{(-1)^{(n-1)/2}}{n^2}\sin(n\omega_0 t) \tag{3}$$

The amplitude of the n-th harmonic scales as $1/n^2$. The amplitude of the fundamental component ($n = 1$) is given by

$$I_{coil}(\omega_0) = \frac{V_{BB}(4/\pi)}{\omega_0 L} \tag{4}$$

In most cases the harmonics have no measurable effect on spin dynamics, which is entirely controlled by the fundamental component. However, they do increase the power dissipated in the coil by $(\pi^2/8 - 1) = 23.4\%$.

The current delivered by the non-resonant transmitter for a given power supply voltage is inversely proportional to $\omega_0 L$, the impedance of the coil. The fundamental component of the coil current creates a circularly-polarized B_1 field for manipulating spins. Since the magnitude of this field is proportional to $I(\omega_0)$, the nutation frequency $\omega_1 = \gamma B_{1c} \propto \gamma V_{BB}/(\omega_0 L)$. The length of a pulse with a given flip angle θ is equal to θ/ω_1, i.e., scales as $\omega_0 L/(\gamma V_{BB}) = B_0 L/V_{BB}$. Thus, for a given static magnetic field and coil geometry, pulse lengths are independent of γ and identical for all NMR nuclei.

When $D < 1/4$ the transmitter enters the DCM. The amplitude of the fundamental component is then given by $I_d(\omega_0) = I(\omega_0)\sin(\pi D)$, and becomes a function of the duty cycle. Therefore we can generate shaped pulses from a constant power supply voltage V_{BB} by varying the duty cycle as a function of time. This process is known as duty-cycle or pulse-width modulation. It is commonly used in class-D audio amplifiers and other nonlinear power amplifier circuits. The range of applicability of this technique is determined by the fact the control pulses must remain long enough to be able to turn the switches on. This condition may be expressed as $2\pi D/\omega_0 > t_{min}$, where t_{min} is the duration of the shortest allowable control pulse. As a result, we cannot use duty-cycle modulation to control the output amplitude over a wide range at high frequencies where the ratio D/ω_0 becomes small and results in very short control pulses.

An important issue with the non-resonant transmitter is high-frequency ringing of the coil voltage, which is caused by resonance between the coil and the output capacitance C_{oss} of the MOSFET switches when all the switches are off and the coil is floating. Such ringing increases the dead-time of the receiver and can damage the switches in the duplexer by causing their voltage ratings to be exceeded. It can be decreased to an acceptable level by using a *snubber* circuit connected in parallel with the switches. Snubbers consist of capacitors, resistors, and diodes, and are designed to dissipate high-frequency energy. Alternatively, the MOSFET drive waveforms shown in Fig. 2 can be modified to ensure that at least two of the switches are on at all times, so that the coil is never floating.

The non-resonant circuit is completely impedance-mismatched from a power-transfer point of view, i.e., nearly 100% of power is reflected from the probe. The energy supplied to the coil to create the B_1 field is almost completely withdrawn during the same RF cycle, and the rest is dissipated in the coil resistance. A tuned probe that uses the same coil to generate the same B_1 field will dissipate approximately the same amount of energy. However, in this case the energy build-up and decay processes will be spread out over approximately Q RF cycles, which reduces the steady-state transmitter current (or voltage) by a factor of Q. Thus the non-resonant approach places greater demands on the voltage, current, and power ratings of the MOSFET switches and other transmitter circuits. In return, it provides all the benefits of a very broadband system, such as arbitrary frequency and phase, fast pulse rise and fall times, and rapid frequency and phase switching. In addition, because the frequency and phase of the coil voltage is fully controlled by the timing of the switches, the RF pulses are accurate and reproducible independent of coil loading due to samples and the environment.

2.2. Duplexer

Broadband duplexers rely on actively-controlled switches to isolate the receiver from the transmitter during RF pulses. The switches can be voltage-controlled, such as BJT or FET transistors and electromechanical relays, or current-controlled, such as PIN diodes. The key figure of merit for any switch is $1/(R_{on}C_{off})$, the inverse product of the resistance in the on-state and the capacitance in the off-state. This quantity tends to be constant for switches made using a particular technology, since any changes that decrease R_{on} (such as making the contacts wider) tends to increase C_{off}, and thus decrease the off-state impedance $1/(\omega_0 C_{off})$. The value of R_{on} should be minimized to prevent it from contributing noise, while that of C_{off} should be minimized to prevent the transmitted pulse from feeding through into the receiver, saturating it, and increasing its dead time. In resonant systems the impedance level is passively increased by the tuned probe circuit before the duplexer, so switches with fairly large R_{on} can be used without degrading the receiver noise figure. This benefit is not available for non-resonant systems, unless the tuned circuit is replaced with a broadband transformer. However, in this case the transformer must be able to withstand the full coil voltage, which is often difficult or impossible. We will therefore assume that the duplexer is directly connected to the coil.

We have evaluated different switch technologies for their performance in broadband duplexers. PIN diodes have very high figures of merit, but are difficult to drive, particularly at low frequencies. Electromechanical relays also have very high figures of merit (typically, two orders of magnitude higher than state-of-the-art semiconductor switches). However, they suffer from slow switching times (at least 100 μs), which limits key NMR pulse sequence parameters such as minimum echo spacing. In addition, they are susceptible to mechanical vibrations and shocks, exhibit prolonged ringing in external magnetic fields, and are typically rated for a billion or fewer switching cycles. We therefore decided to focus on semiconductor switches.

Our duplexer consists of two FET switches connected back-to-back that isolate the receiver when the transmitter is ON, and a pair of cross-coupled diodes that isolate the transmitter from the coil when it is OFF, as shown in Fig. 4. Each FET can only block positive drain-source voltages, because the intrinsic or body diode turns on when the voltage becomes negative. Thus two back-to-back FETs are needed to block the transmitter voltage, which is bidirectional in nature. In addition, the FET gate driver must generate a control voltage V_{GS} between the gate and source terminals of the FETs that is independent of the actual voltage on these terminals with respect to ground. As a result, the driver must be magnetically or optically isolated from the rest of the electronics. Magnetic isolation using a transformer is only effective for AC signals, and is thus limited to short acquisition times. We used optical isolation to avoid this problem. The output of the optical isolator is powered by a floating battery V_{DUP}. It controls an H-bridge circuit that sets the FET gate-source control voltage to $+V_{DUP}$ or $-V_{DUP}$ during the duplexer ON and OFF states, respectively. The on-state resistance and off-state capacitance of the circuit are $2R_{on}$ and C_{oss}, respectively. Here R_{on} and C_{oss} are the on-resistance and output capacitance of each FET switch.

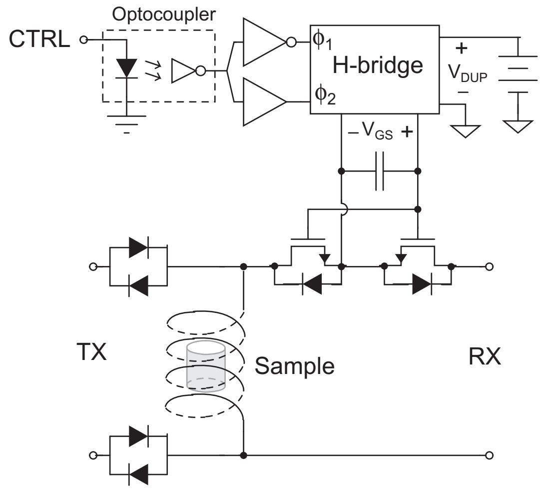

Fig. 4. Simplified circuit diagram of the broadband duplexer circuit.

2.3. Receiver

The basic metric for quantifying the performance of any receiver is its noise figure (NF), which is defined as the ratio of input SNR to output SNR. In a MR system the input (or intrinsic) SNR depends on B_0 field strength, the pulse sequence, transmitter and receiver coil design, sample losses, and other factors [15]. In this section we will assume that the input SNR remains constant, and focus on maximizing the output (final) SNR by minimizing receiver NF.

A variety of circuit techniques exist for obtaining very low NF at a particular frequency, or over a small range of frequencies [16]. Such narrow band techniques rely upon the use of noiseless reactive elements (inductors and capacitors) to provide voltage gain before the active preamplifier. The resultant resonant circuits act as impedance transformers over a narrow range of frequencies around ω_0, the resonant frequency. For example, a parallel LC circuit removes the reactive component of the coil impedance $Z_L = j\omega_0 L + R$ at resonance while increasing the resistive component by a factor of Q^2, where $Q = \omega_0 L/R$ is the quality factor of the coil at the resonant frequency. This transformation provides a significant, *noiseless* voltage gain of $Q \gg 1$ for both the received NMR signal and associated noise sources, such as the coil and sample. As a result, the noise contributed by the active preamplifier becomes less significant, i.e., the receiver NF decreases. Such tuned (but not impedance-matched) probes are often used when the preamplifier has very high input impedance and cable lengths are much shorter than the wavelength, i.e., at relatively low frequencies.

At higher frequencies, it is often convenient to match the output impedance of the probe to a characteristic real impedance Z_0. The voltage gain for the received signal near resonance is then given by $(1/2)\sqrt{Z_0/R} = (1/2)\sqrt{Z_0 Q/(\omega_0 L)}$. i.e., the square root of the impedance transformation ratio times a factor of $1/2$. In this tuned-and-matched case the probe voltage gain is lower, but usually still high enough to achieve a low receiver NF. In addition, the NF is independent of the receiving coil's characteristics, as the latter's impedance has been transformed to the constant value Z_0 (usually 50 Ω). However, tuned circuits only provide low NF over a limited range of frequencies: The noise-matching bandwidth is $\approx \omega_0/Q$ in the tuned case and $\approx 2\omega_0/Q$ in the tuned-and-matched case. Here Q is usually equal to the quality factor of the coil, but can be lowered below this value (without introducing additional noise) through active-damping circuits [17].

We decided not to use conventional tuning and matching techniques, since they are unsuitable for ultra-broadband receivers. However, in the absence of tuning and matching the impedance of the probe will necessarily depend on that of the receiving coil. It follows that NF will be a complicated function of coil and other impedances, and we must therefore proceed from first principles in assessing SNR. A detailed NF analysis of our system is presented in this section.

Instead of a tuned circuit, our system uses a transformer with a ferromagnetic core to provide *broadband* passive, low-noise voltage gain (determined by the turn ratio n) before the preamplifier. Transformer-coupled topologies can produce low NF over a wide frequency range [18]. Their main disadvantage is that the reactive part of the coil impedance is not removed, and instead presents a large inductive load to the first stage preamplifier. The result is a large source impedance at high frequencies, which makes the circuit sensitive to current noise and also limits its useful bandwidth. A commercial example of a transformer-coupled preamplifier is the SR-554 (Stanford Research Systems). It uses a specially-wound transformer with a turns ratio of 1:100 to amplify the input signal above the noise floor of a standard FET-input operational amplifier. The result is very low input-referred noise (0.1 nV/Hz$^{1/2}$, corresponding to a 0.6 Ω resistor at 300 K) but only at frequencies up to several kHz. Other potential disadvantages of the transformer include ringing from the ferromagnetic core following RF pulses, saturation of the core by nearby static magnetic fields (which can be reduced by adding magnetic shielding), and increased noise and signal losses at high frequencies [19]. Nevertheless, transformers remain a viable design option at frequencies up to several MHz (or possibly several tens of MHz in the case of small RF coils).

2.3.1. Transfer function

In the case of our transformer-coupled receiver the NMR coil, which has inductance L and series resistance R, is connected across the primary side of the transformer. The inductances of the primary and secondary transformer windings are denoted by L_1 and L_2, while R_1 and R_2 are their series resistances, $0 < k < 1$ is their coupling constant, and $n_{eff} = k\sqrt{L_2/L_1} \approx kn$ is the effective turns ratio. For transformers with ferromagnetic cores, $k \approx 1$ and $n_{eff} = n$, the geometric turns ratio.

The transfer function of our receiver with the NMR coil and transformer connected is shown schematically in Fig. 5. The effective source impedance behaves as an inductor of value

$$L_{eff} \approx n_{eff}^2 \left(\frac{L_1}{L + L_1}\right) L, \qquad (5)$$

while the receiver input impedance behaves as a capacitance of value C_{eff}. The factor of $L_1/(L + L_1)$ is a result of the voltage divider formed by the NMR coil and the primary winding of the transformer. Its effect can be minimized by increasing L_1, i.e., using a transformer with a high-permeability core. Thus the transformer increases the effective source impedance by a factor of approximately $n_{eff}^2 L_1/(L + L_1)$. The result is a band-pass transfer function. The lower cut-in frequency is approximately the inverse of the L–R time-constant τ_1 of the input circuit consisting of the NMR coil, duplexer and primary winding of the transformer T_1, while the upper cut-off frequency is approximately equal to the L–C resonance frequency between L_{eff} and C_{eff}:

$$\omega_{T1} \approx \frac{R + R_{dup} + R_1}{L + L_1}$$
$$\omega_h = \frac{1}{\sqrt{L_{eff} C_{eff}}} \approx \frac{1}{n}\sqrt{\frac{(1/L + 1/L_1)}{C_{eff}}}. \qquad (6)$$

Here $R_{dup} \approx 2R_{on}$ is the resistance of the duplexer in the "on" state. In practice the low-frequency gain may also be determined by inter-stage coupling networks in the preamplifier. These networks act as high-pass filters for the NMR signal with a cut-in frequency of ω_{CC} that can be set by the designer.

The upper cut-off frequency ω_h is approximately equal to the maximum useful operating frequency of the receiver. At frequencies higher than ω_h the LC filter formed by L_{eff} and C_{eff} cuts off and the voltage gain before the preamplifier decreases from its low-frequency value of n as $1/\omega^2$. As a result the input-referred noise of the receiver increases approximately as ω^2. The ratio between ω_{T1} and ω_h can be very large in practical designs, resulting in a very broadband receiver. However, the high-Q resonance at ω_h results in long-lived ringing that increases the settling time after RF pulses. Such ringing can be suppressed by an active feedback circuit once its amplitude becomes smaller than that circuit's linear range (typically tens to hundreds of mV). We have used an active damping technique described by Hoult [17] for this purpose. The method uses capacitive feedback to the input of the preamplifier. It can be shown that a capacitor of value C_f in series with an integrator feedback function $H(\jmath\omega) = A/(\jmath\omega\tau)$ behaves as a resistor of value R_{damp} connected between the preamplifier input and ground, where

$$R_{damp} = \frac{\tau}{AC_f}. \qquad (7)$$

Importantly, the damping resistor, which is shown in Fig. 5, adds very little noise because it is created with an almost noiseless capacitor. Hence active damping is preferable to passive damping with a normal (noisy) resistor. In our case the gain A is provided by the preamplifier itself, while an op-amp-based integrator circuit provides the rest of the feedback function. The damped Q at ω_h is

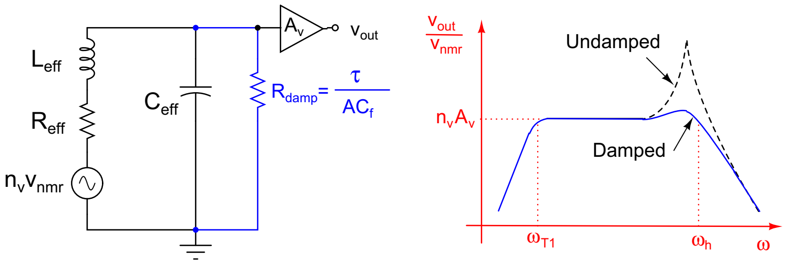

Fig. 5. Simplified model of the receiver transfer function with and without active damping.

given by $Q_{damp} \approx R_{damp}/\sqrt{L_{eff}/C_{eff}}$. The value of R_{damp} is chosen to keep $Q_{damp} \approx 1$, resulting in very little peaking in the receiver transfer function.

2.3.2. Noise analysis

The noise model of a generic amplifier is shown in Fig. 6(a). It consists of an input signal source v_{in} with source impedance Z_s, a noiseless amplifier with voltage gain A, and input-referred noise voltage and current sources (e_n and i_n, respectively). The application of this generic model to our NR preamplifier is shown in Fig. 6(b). The source impedance Z_s now consists of the NMR coil, represented by the inductor L and series resistance R, and a 1:n step-up transformer (T_1). The primary and secondary winding inductances of the transformer are represented by L_1 and $L_2 \approx n^2 L_1$, respectively, while its winding resistances are represented by R_1 and $R_2 \approx nR_1$.

For simplicity, we will assume that correlations between the noise voltage and current sources (e_n and i_n, respectively) can be neglected. This is usually a good approximation at all frequencies of interest. The power spectral density (PSD) of the noise voltage at the amplifier input terminal is then given by

$$\overline{v_{ni}^2} = \overline{v_{ns}^2} + \overline{e_n^2} + |Z_s|^2 \overline{i_n^2}. \tag{8}$$

Here $Z_s \approx n^2(i\omega L + R)$ and $\overline{v_{ns}^2}$ are the effective impedance and voltage noise PSD, respectively, of the input signal source after passing through the step-up transformer. The noise figure (NF) of the amplifier is then given by

$$NF = \frac{\overline{v_{ni}^2}}{\overline{v_{ns}^2}} = 1 + \frac{\overline{e_n^2} + |Z_s|^2 \overline{i_n^2}}{\overline{v_{ns}^2}}. \tag{9}$$

The goal of an optimal amplifier design is to minimize NF over a wide range of frequencies. This goal can be achieved by minimizing the quantity $\overline{e_n^2} + |Z_s|^2 \overline{i_n^2}$, which is known as the input-referred noise PSD of the amplifier.

The input-referred noise of a well-designed amplifier is largely determined by a single input transistor, typically a BJT, JFET, or MOSFET. This device produces both frequency-independent thermal noise and low-frequency “flicker” or 1/f noise. The importance of 1/f noise can be estimated through the corner frequency ω_c, which is defined as the frequency at which the power spectral densities of thermal and 1/f noise are equal to each other. The minimum useful operating frequency ω_l of the receiver is approximately equal to the largest of three frequencies: ω_{T1} (set by the input transformer), ω_{CC} (set by inter-stage coupling networks in the preamplifier), and ω_c (set by 1/f noise from the input transistor).

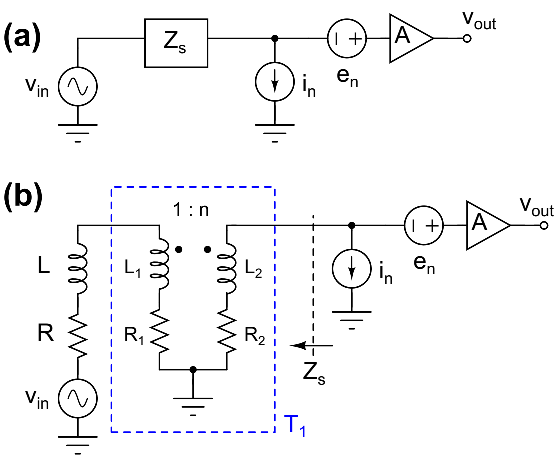

Fig. 6. Simplified circuit model of (a) a generic noisy amplifier, and (b) the NR preamplifier.

We decided to use a silicon JFET as the input device because it has very low input current noise, as well as low 1/f noise ($\omega_c \approx 1$ kHz at typical biasing conditions). BJTs are not suitable for this application because they have relatively large base currents, which generate input current noise, and may also have large intrinsic base resistances, which generate input voltage noise. Similarly, high electron mobility transistors (HEMTs) are not suitable because of very high levels of 1/f noise.

The input capacitance C_{eff} of a well-designed receiver is usually dominated by that of the input transistor. This quantity should be minimized to increase ω_h, i.e., maximize the receiver bandwidth. The input capacitance of a JFET is usually dominated by C_{gs}, its intrinsic gate-source capacitance. In order to reduce the receiver input capacitance C_{eff} and increase ω_h we configured the FET as a source-follower, as shown in Fig. 7. This circuit acts as a unity-gain buffer with low output impedance. As a result, the voltage across C_{gs} is approximately zero, effectively eliminating its effects. The input capacitance is then dominated by C_{gd}, the intrinsic gate-drain capacitance. Fortunately $C_{gd} \ll C_{gs}$ as long as the transistor is biased in the saturation region. In addition, C_{gd} is voltage-dependent. Its value can be somewhat reduced by increasing the power supply voltage V_{dd}, at the expense of increased gate leakage current (which results in increased input current noise), and also power consumption.

The source-follower circuit only provides a voltage gain of 1, so we still need a low-noise amplifier stage after it. Fortunately the buffering provided by the source-follower makes the input capacitance of this stage unimportant. We can get voltage gain $A_v > 1$ from this stage by using M JFET devices in parallel in a common-source stage, as shown in Fig. 7(a). Alternatively we can use a 1:N step-up transformer before a common-source stage with voltage gain $A_v > 1$, as shown in Fig. 7(b). The voltage gain provided by the transformer T_2 is almost noiseless, resulting in lower noise (and power consumption) for the latter circuit. This may be seen by comparing the total input-referred voltage noise of the two circuits:

$$\begin{aligned}\overline{e_n^2} &= \frac{4kT\gamma}{g_m}\left[1 + \frac{1}{M}\left(1 + \frac{1}{\gamma A_v}\right)\right] \qquad \text{circuit(a)},\\ &= \frac{4kT\gamma}{g_m}\left[1 + \frac{1}{N^2}\left(1 + \frac{1}{\gamma A_v}\right)\right] \qquad \text{circuit(b)}.\end{aligned} \tag{10}$$

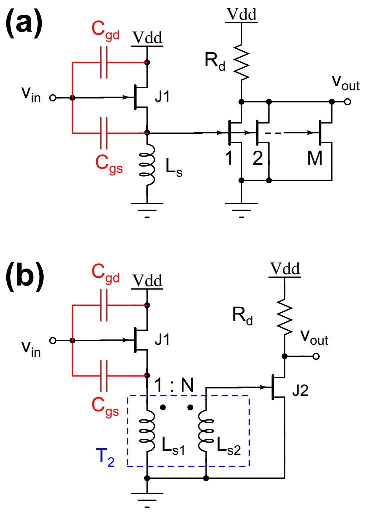

Fig. 7. Simplified front-end circuit of the NR receiver, with voltage gain after the input buffer being provided by (a) a common-source amplifier, or (b) a step-up transformer T_2. The input transformer (T_1) is not shown.

In both cases the first term is contributed by the input buffer, the second by the JFET(s), and the third by the resistor R_d. In addition, g_m is the small-signal transconductance of each JFET, and $\gamma \approx 2/3$ for long-channel JFETs. Ideally we would like the total input-referred voltage noise to approach that of the input JFET alone. Eq. (10) shows that this goal can be achieved by using many devices in parallel ($M \gg 1$) or with a moderate transformer turns ratio ($N > 1$). The noise from the input JFET can be reduced by increasing its bias current I_d, which increases $g_m \propto \sqrt{I_d}$, but at the expense of increased power consumption.

For frequencies between ω_l and ω_h, a complete analysis shows that the effective source voltage and impedance during NMR signal reception are given by v_s and $Z_s = \jmath\omega L_{eff} + R_{eff}$, where

$$\begin{aligned} v_s &= n_{eff}\left(\frac{L_1}{L+L_1}\right)v_{nmr} \equiv n_v v_{nmr}, \\ L_{eff} &= n_{eff}^2\left(\frac{L_1}{L+L_1}\right)L + L_2\left(1-k^2\right), \\ R_{eff} &= n_{eff}^2\left(\frac{L_1}{L+L_1}\right)(R+R_{dup}+R_1)+R_2. \end{aligned} \tag{11}$$

Here v_{nmr} is the voltage induced by spins on the NMR coil, $n_v = n_{eff}/(1+L/L_1)$ is the net voltage gain produced by the input transformer T_1, and R_{dup} is the resistance of the duplexer in the "on" state. The transformer also contributes additional source impedance in the form of "leakage" inductance $L_2\left(1-k^2\right)$ and winding resistances. Leakage inductance is minimized for transformers with high-permeability ferromagnetic cores, which have $k \approx 1$ and $n_{eff} \approx n$.

For convenience we also define the following quantities: $Q_s \equiv \omega L_{eff}/R_{eff}$, the quality factor of the source impedance, $R_e \equiv \overline{e_n^2}/(4kT)$, the input-referred noise resistance of the preamplifier, and $R_n \equiv \sqrt{\overline{e_n^2}/\overline{i_n^2}}$, the optimal source resistance for minimizing NF, i.e., for noise matching. The NF of the transformer-coupled receiver over the useful bandwidth (between ω_l and ω_h) is then given by

$$\begin{aligned} NF &= \frac{(R+R_{dup}+R_1)n_v^2+R_2+R_e\left[1+\left(\frac{Q_sR_{eff}}{R_n}\right)^2\right]}{n_v^2R}, \\ &\approx 1+\underbrace{\frac{R_{dup}}{R}}_{\text{Duplexer}}+\underbrace{\frac{R_1}{R}\left[1+\frac{(1+L/L_1)^2}{n_{eff}}\right]}_{\text{Transformer}}+\underbrace{\frac{R_e(1+L/L_1)^2}{n_{eff}^2R}\left[1+\left(\frac{Q_sR_{eff}}{R_n}\right)^2\right]}_{\text{Preamplifier}}. \end{aligned} \tag{12}$$

The first term in the expression for NF is equal to 1. It corresponds to the noise of the receiving coil. The second, third, and fourth terms correspond to noise added by the duplexer, transformer, and preamplifier, respectively. In deriving this expression we have assumed that the primary and secondary windings use the same wire, so that $R_2 \approx n_{eff}R_1$. Within the third term, the first sub-term is contributed by the primary side of the transformer, while the second sub-term is contributed by the secondary side. We see that the latter can be neglected if $n_{eff} \gg 1$. This behavior occurs because the ratio of signal voltages across the transformer is $\propto n_{eff}$, but the ratio of noise voltages contributed by the windings is $\propto \sqrt{R_2/R_1} = \sqrt{n_{eff}}$.

The final term in (12) consists of two sub-terms. The first is due to the voltage noise of the preamplifier, while the second is due to the current noise. The effects of current noise increase rapidly at high frequencies and for large values of L_{eff}, which result in large values of Q_s. Thus, this source of noise places upper limits on both the coil inductance and bandwidth of the amplifier.

Eq. (12) allows us to predict the preamplifier noise properties, i.e., the parameters R_e and R_n, and optimize its performance. Ideally we want R_e to be small (low voltage noise) and R_n to be large (current noise much smaller than voltage noise, resulting in constant NF between ω_l and ω_h). For a given transformer, increasing the NMR coil inductance L lowers the effective voltage gain $n_v = n_{eff}/(1+L/L_1)$ before the preamplifier. As a result, the NF increases, as shown in Eq. (12). The value of n_{eff}, the effective transformer turns ratio, affects the maximum operating frequency and noise figure of the receiver in similar ways, as shown in Eqs. (6) and (12), respectively. Increasing n_{eff} lowers the receiver NF, but also ω_h, resulting in a smaller useful frequency range. This trade-off between coil inductance, noise figure, and maximum operating frequency is shown in Fig. 8. It is fundamental for non-resonant receivers, and is ultimately a result of the frequency-dependent reactance of the coil.

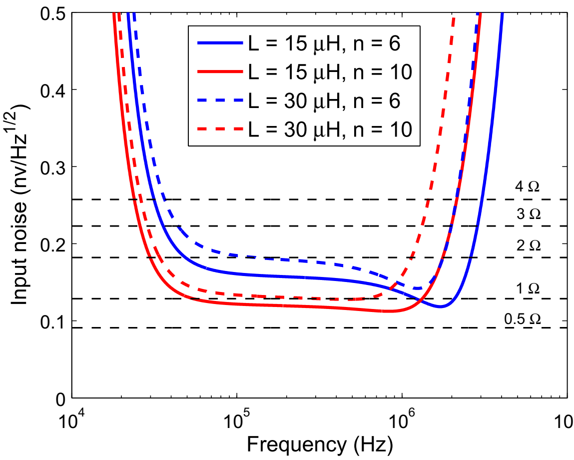

Fig. 8. Simulated input-referred noise of our non-resonant receiver as a function of frequency for various values of coil inductance L and transformer turns ratio n. The transformer T_1 was assumed to have a primary winding inductance of $L_1 = 56$ μH. We also assumed the preamplifier circuit shown in Fig. 7(b), with a turns ratio of $N = 6$. The thermal noise of resistors at 300 K is also shown for comparison.

The input-referred noise of the receiver increases at frequencies below ω_l, the lowest operating frequency, as shown in Fig. 8. The lowest operating frequency of our current NR receiver design is equal to ω_{CC} (which is set by inter-stage high-pass coupling networks within the preamplifier) since this is much larger than either ω_{T1} or ω_c. The value of ω_{CC} can be decreased by using larger inter-stage coupling capacitors. However, this circuit modification will be accompanied by slower recovery from input overloads (saturation). In our current design we set $\omega_{CC}/(2\pi) = 60$ kHz, which is high enough to allow the circuit to quickly recover from saturation (<40 μs), but low enough to amplify the lowest Larmor frequency of interest (approximately 100 kHz).

The rest of our receiver consists of broadband voltage gain stages, and high-pass and low-pass filters to provide additional rejection of out-of-band noise prior to digitization. These circuits were implemented with high-speed operational amplifiers.

2.3.3. Recovery from saturation

We have assumed so far that the receiver is operating in a linear or small-signal regime. However, a key attribute of NMR receivers is their recovery from saturation following RF pulses. Receiver recovery time must be minimized because it often limits important pulse sequence parameters, such as the minimum possible echo period T_E. It typically consists of several components in addition to the gain recovery or settling time of the receiver itself, including the decay time of magnetic energy stored in the coil (pulse ring-down) and mechanical oscillations of metallic parts of the probe (magnetoacoustic ringing). The stored coil energy at the end of a

Table 1
Key circuit components.

Component	Manufacturer	Part number	Notes
H-bridge switch	Fairchild	FDD6N20TM	MOSFET, 200 V, 4 A, $R_{on} = 0.8\ \Omega$
H-bridge driver	International Rectifier	IRS2011	Half-bridge, 200 V, 1 A
Duplexer switch	EPC	EPC2012	GaNFET, 200 V, 3 A, $R_{on} = 0.1\ \Omega$
Optical isolator	Avago	ACPL-074L	
Input transformer (T_1)	Mini-circuits	T36-1-KK81	$n = 6,\ L_1 = 56\ \mu\text{H}$
Input transistor	NXP	BF862	JFET, $g_m \approx 45$ mS at $I_D = 15$ mA
Second stage transformer (T_2)	Mini-circuits	T36-1-KK81	$N = 6,\ L_1 = 56\ \mu\text{H}$

Table 2
Key performance metrics.

Parameter	Symbol	Value
Static field	B_0	Variable (fringe field)
Probe size		Cylindrical, ID = 5.5 cm, length = 8.8 cm
Coil inductance	L	15 μH
Transmitter voltage	V_{BB}	0–200 V
Receiver bandwidth	f_l–f_h	80 kHz to 2.2 MHz
In-band receiver gain		> 62 dB

pulse also resonates with parasitic capacitances in the system, causing ringing that decays with a time constant τ_1. However, these modes occur at much higher frequencies than the Larmor frequency and can be easily filtered out during later signal processing. In other words, our non-resonant system does not possess a natural mode of oscillation of the coil voltage near the Larmor frequency, which greatly reduces the pulse ringdown component.

We paid careful attention to our receiver circuit design to minimize its settling time after saturation. Large inter-stage coupling capacitors often cause slow settling, because the currents that charge or discharge them can get shut off during saturation. We minimized the number and size of such capacitors. Secondly, the feedback damping circuit only operates as designed when the receiver is linear, and in principle can ring or go unstable for large input signals. We studied this problem by performing extensive circuit simulations, and reduced A, the voltage gain of the first receiver stage, to eliminate it. The lowest practical value of A is determined by the requirement that noise from later receiver stages does not substantially increase the overall input-referred noise. Finally, the settling time can be minimized by limiting the input voltage during RF pulses and increasing the linear range of the receiver. We limited the receiver input voltage to approximately ±800 mV with a pair of cross-coupled diodes. We also increased its linear range by increasing the bias current I_D of the JFETs shown in Fig. 7. Unlike BJTs, which have a fixed linear range of $kT/q = 25.9$ mV at room temperature, the linear range of FETs increases $\propto \sqrt{I_D}$. Thus burning more power increases the linearity of our receiver as well as decreasing its input-referred noise.

2.4. Hardware implementation

A list of important circuit components in our current implementation of the non-resonant MR system is shown in Table 1. We used enhancement-mode gallium nitride transistors (GaNFETs) from EPC (El Segundo, CA) for the duplexer switches because they have a significantly better figure of merit $1/(R_{on}C_{off})$ than comparable silicon MOSFETs. We also selected the excellent BF862 JFET from NXP as the input transistor in the preamplifier. At room temperature and typical biasing conditions ($V_{GS} = 0,\ V_{DS} = 4$ V) this device has input-referred voltage and current noise PSDs of 0.8 nV/Hz$^{1/2}$ and 1.0 fA/Hz$^{1/2}$, respectively, thus resulting in a noise-matching resistance $R_n \approx 0.8$ MΩ.

All components were integrated onto a printed circuit board (PCB) with four wiring layers. A photograph of the assembled board, which has two independent RF input channels labeled CH1 and CH2, is shown in Fig. 9. An external signal (labeled MOD) can be used to control the transmitter threshold voltage $V_{\pm}$, thus making it possible to generate shaped pulses via duty cycle modulation. Table 2 shows important performance metrics of our system.

All the measurements reported in this paper were made using a solenoidal sample coil with ID = 5.5 cm and length = 8.8 cm. It consisted of 27 turns of AWG 16 magnet wire wound around a Teflon form with variable pitch ($\sim$4 mm at the center, $\sim$2 mm at the edge) to improve B_1 homogeneity. The self-inductance was $L = 15\ \mu\text{H}$ after assembly inside a tight shield box, resulting in an effective transformer voltage gain of $n_v = 4.7$ before the preamplifier. The shield is necessary for reducing pickup from AM radio stations, switching power electronics, and other sources of external RF interference in this frequency range. However, it also generates eddy currents that lower the measured coil Q to 20 at 100 kHz and 50 at 2 MHz. The coil was connected to the board using 2 m of balanced (twin conductor) coaxial cable and twin BNC connectors.

The voltage gain of the receiver was measured to be > 62 dB between 80 kHz and 2.2 MHz, in good agreement with simulations, as shown in Fig. 10. This figure also shows the measured input-referred noise with the coil connected. This quantity is also in very good agreement with simulations, and is lower than the thermal noise of a 2 Ω resistor for frequencies between 40 kHz and 2.0 MHz, i.e., over a 1:50 frequency range. Most of this noise is contributed by the preamplifier, which used the circuit shown in Fig. 7(b) with $N = 6$.

Measured *output* noise from the non-resonant receiver is shown in Fig. 11(a) for 3 cases:

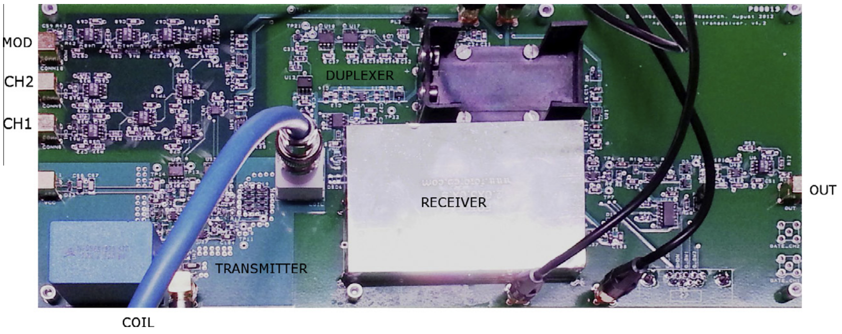

Fig. 9. Layout of the transceiver circuit board, measuring 25.1 cm × 10.9 cm in size.

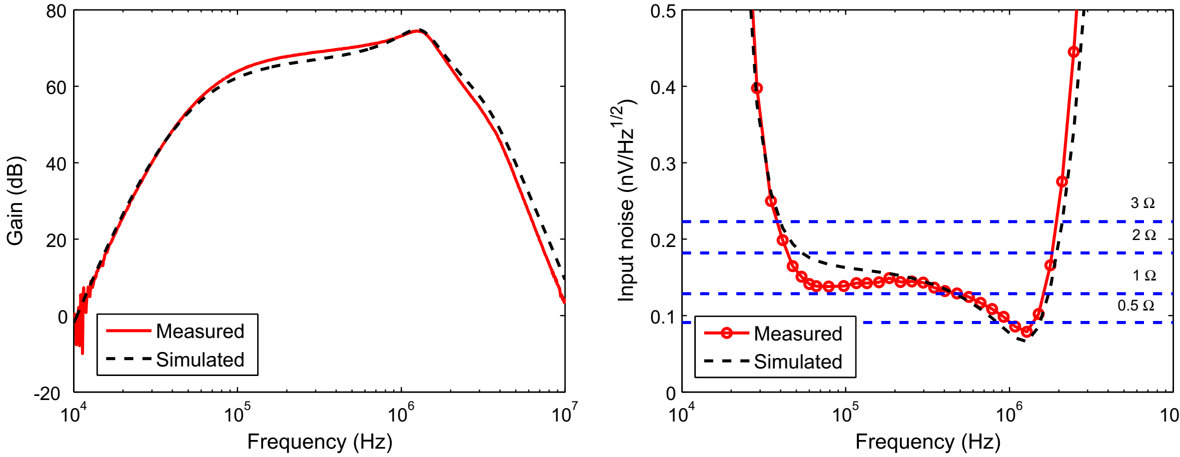

Fig. 10. Measured voltage gain (left) and input-referred noise (right) of our non-resonant receiver as a function of frequency for $L = 15\ \mu H$ and $n = 6$. The expected gain and noise based on circuit simulations and the thermal noise of resistors between 0.5 Ω and 3 Ω at room temperature are also shown for comparison.

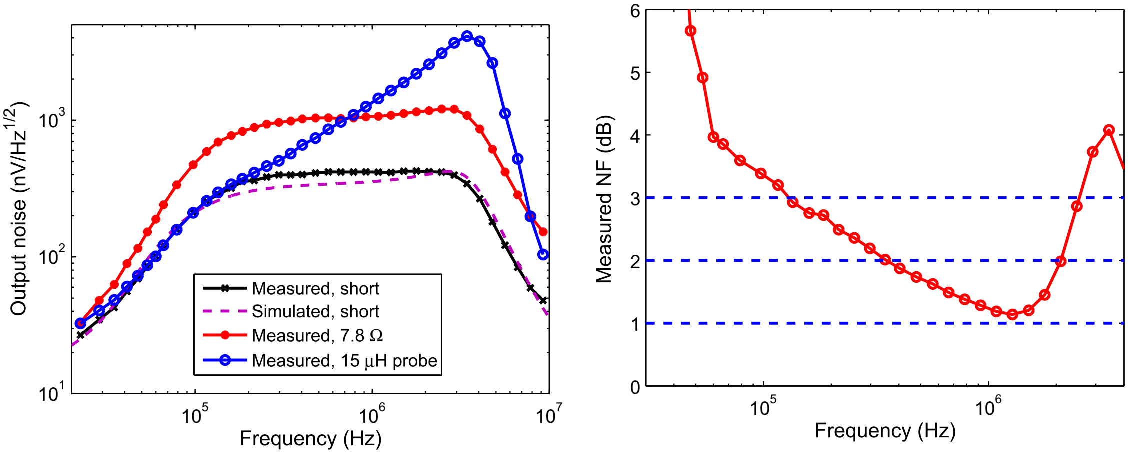

Fig. 11. Measured noise PSD at the output of the NR receiver with various input terminations (left), and the measured receiver NF (right).

1. Amplifier input shorted to ground (no source noise).
2. A 7.8 Ω resistor connected across the amplifier inputs.
3. The NMR probe coil (ID = 5.5 cm, length = 8.8 cm, inductance = 15 μH) connected across the amplifier inputs.

The output noise (with the input shorted) predicted by a circuit simulation of the receiver is also shown for comparison. It matches the measured curve for case (1) quite well. The current noise of the input JFET is negligible at room temperature, so all additional noise visible in cases (2) and (3) must have been contributed by the load resistor or coil, respectively.

The resistor adds broadband noise over the entire amplifier bandwidth, as expected (see curve (2)). The coil adds very little noise at low frequencies, as expected (see curve (3)). However, its noise contribution rapidly increases with frequency, because of 2 reasons. Firstly, the coil's effective series resistance increases because of skin effect. More importantly, the parasitic capacitance in parallel with the coil amplifies its noise, as in a normal resonant probe, with the maximum amplification occurring at its self-resonant frequency (approximately 3.5 MHz in this case). Such resonant amplification of noise happens even though the active damping circuit in the receiver suppresses this resonance from the signal transfer function. Since the active damping circuit adds no noise of its own, it removes the unwanted resonance from the signal transfer function while maintaining very low input-referred noise near the original resonant frequency.

To summarize, Fig. 11(a) shows that most of the output noise of the non-resonant receiver comes from the probe coil for frequencies $>$ 250 kHz. As a result, the NF of the receiver should be low over a broad range of frequencies. We confirmed this statement by directly measuring the frequency-dependent series resistance R of the sample coil with a network analyzer. The receiver NF can then be computed using Eq. (9) and the input-referred noise data shown in Fig. 10. The results are shown in Fig. 11(b). They confirm that the receiver NF with this relatively low-Q sample coil is less than 3 dB over a 1:19 frequency range (130 kHz to 2.5 MHz). Hence our NR receiver demonstrates very broad reception bandwidth with competitive noise performance (less than a factor of 2 increase in averaging time) compared to conventional narrowband MR receivers in this frequency range.

3. Applications

We have used our system for NMR experiments in the fringe field of a 2 T superconducting magnet. Relaxation and diffusion measurements have been successfully performed for Larmor frequencies between 98 kHz and 3.2 MHz with no hardware tuning.

The length of a $\pi/2$ pulse at full transmitter power ($V_{BB} = 200$ V) with the present coil at 1 MHz was approximately 18 µs, which corresponds to $\omega_1 \approx 2\pi \times 13.9$ kHz and is in good agreement with theoretical predictions. The receiver recovery time was measured to be less than 40 µs over this entire frequency range. Measurements of long-T_2 samples such as benzene and distilled water match expected values, showing that the transmitted RF pulses are stable in both amplitude and phase.

3.1. Imaging, multi-slice, and multi-nuclear measurements

One key advantage of a broadband system is that the RF frequency can be easily changed, because the hardware does not need to be modified or re-tuned in any way. Consider the case, common in *ex-situ* NMR, where the excited sample volume is power-limited by large sample size and/or inhomogeneous magnetic field. We can then easily switch frequencies to move the region of investigation (often called the slice). In our case the field gradient extends along the depth, or z-dimension, resulting in slice thicknesses of a few mm. As a result, we can scan through different depths by dynamically varying the RF frequency. We refer to this process as depth profiling or 1D imaging. Using the broadband system, switching to different nuclei also becomes trivially simple without adjustment of the hardware system. Fig. 12 shows measured 1D profiles of proton and sodium signals from a 250 ppK brine solution in a cylindrical sample bottle of diameter $d = 4.5$ cm. The shapes of these curves are consistent with the known 1D spatial profile of the sample.

Multi-slice experiments are inconvenient at low frequencies with a tuned probe because the probe bandwidth ω_0/Q, where Q is the quality factor of the RF coil, is often comparable to ω_1, the excitation bandwidth. Multi-slice operation then requires re-tuning of the probe hardware at every step, which is typically a slow process. This requirement can be completely avoided using our setup, which therefore enables a multi-slice approach to many time-consuming experiments that is similar to well-known fast imaging methods used in high-field MRI.

For example, in order to measure diffusion, several acquisitions have to be made with different diffusion weightings. In a conventional single-slice technique, substantial waiting time is necessary in between different scans in order for the spin system to recover its equilibrium. In the multi-slice mode, acquisition can be moved to a different slice without the waiting time, resulting in a significant acceleration of the measurement. A similar approach can be used to accelerate T_1 measurements, and in general any indirect dimension of a multi-dimensional experiment can be encoded in different slices. The multi-slice mode can also be used to simply increase the SNR per unit time by eliminating wait times between scans that are added together. The resulting increase in SNR is particularly significant for samples with large T_1/T_2 ratios.

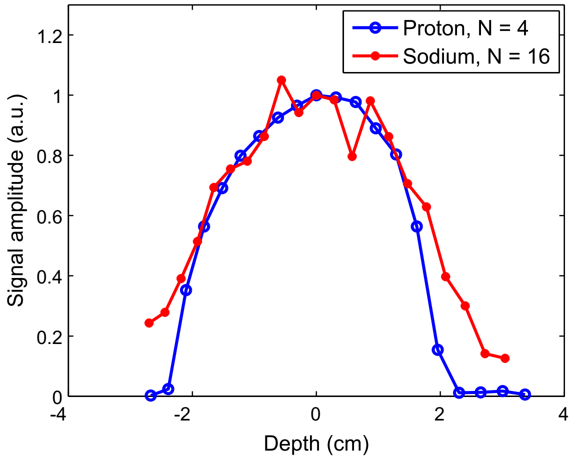

Fig. 12. Measured depth profiles of proton and sodium signals from a 250 ppK brine solution, i.e., 250 gm NaCl dissolved per liter. This results in a Na concentration of 4.3 M, which is 3.9% of the proton density of a pure water sample. The x-axis corresponds to a Larmor frequency range of 1.8–2.2 MHz for protons, and 476–582 kHz for Na. The static field gradient increases from 13.6 G/cm to 17.5 G/cm over this frequency range. Each point in the profiles was calculated by using the CPMG pulse sequence and adding together echoes from N scans.

Our system also allows excitation of very broad spectra using frequency-swept, composite, or phase-modulated pulses. Such broadband pulses allow the excited volume and SNR to be increased in inhomogeneous fields without increasing the peak RF power level [20–22]. Another simple application is measurement of the same sample at different Larmor frequencies. Such experiments are normally performed with expensive field-cycling electromagnets and are limited to T_1 measurements. By contrast, our system allows any NMR experiment to be performed as a function of Larmor frequency.

3.2. Rapid frequency switching

Our system allows very rapid switching of the RF frequency over a range that greatly exceeds the excitation bandwidth ω_1. This ability is of particular interest at low frequencies, because it eliminates the need to re-tune the probe hardware when changing the frequency over a range that exceeds ω_0/Q, as described in the previous section.

For example, our system allows multiple slices to be excited and detected within the same CPMG sequence, as shown in Fig. 13. In this case each excitation and refocusing pulse consists of N_s segments of different frequencies. The flip angle of each segment is $\pi/2$ and π, respectively. The frequency of the n-th segment is given by $f_0 + (n-1)\Delta f_0$, where Δf_0 is the separation between adjacent slices. All pulse lengths and delays can be set to integer multiples of $1/(\Delta f_0)$ to maintain phase coherence within each slice. This constraint can be removed by explicitly tracking the phase of each slice in the rotating frame and appropriately changing the phase of the refocusing pulses. The echoes from each slice form sequentially in time, i.e., separated by T_s, where T_s is the length of each refocusing segment, as shown in Fig. 14. They are easily distinguished from each other by their frequency content. In this case the receiver frequency has been kept constant at the center frequency of the first slice. Thus the first echo has been demodulated to zero frequency (baseband), while the second echo has been demodulated to an offset frequency of $\Delta f_0 = 20$ kHz.

When multiple CPMG sequences are run simultaneously on different slices, one has to take care of the interactions that exist through the Bloch–Siegert (B–S) shift [23]. It can be shown that the application of an RF pulse at an offset frequency $\Delta\omega$ induces an extra phase shift on the transverse magnetization, the so-called B–S phase shift ϕ_{BS}. In the limit where $\Delta\omega \gg \omega_1$, the nutation frequency, this phase shift for on-resonance magnetization can be written as

$$\phi_{BS} = \left(\frac{\theta}{2}\right)\frac{\omega_1}{\Delta\omega}. \tag{13}$$

Here $\theta = \gamma\omega_1 t_p$ is the nominal tipping angle of the pulse, and t_p is its duration. The B–S phase shift will generally cause problems when multiple slices are interleaved as shown in Fig. 14. In general, the sequence will behave as a mixture of CP and CPMG, resulting in rapid signal decay. However, this effect can be taken into account and corrected for by phase shifting the $\pi/2$ excitation pulse for the second and higher slices, as explained below.

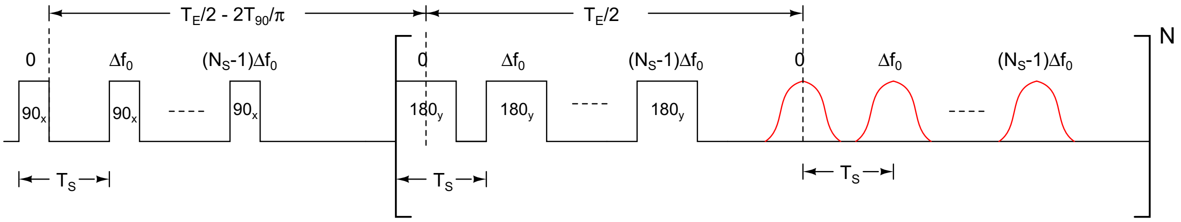

Fig. 13. A multi-slice CPMG pulse sequence.

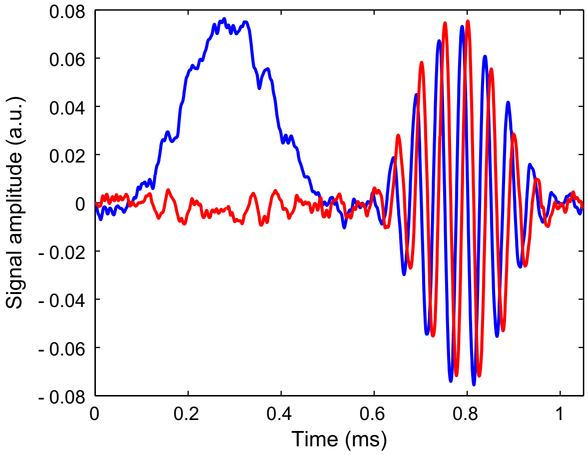

Fig. 14. Experimental data for the multi-slice CPMG pulse sequence with two slices. The sample for the experiment was NiCl solution ($T_2 = 120$ ms). Other experimental parameters include $f_0 = 2.0$ MHz, $T_{90} = 140$ µs, $\Delta f_0 = 20$ kHz, and $T_s = 500$ µs.

The timing in the standard CPMG sequence is adjusted such that the phase acquired between the excitation pulse and the first refocusing pulse is exactly half the phase acquired in each refocusing cycle. This phase is proportional to the Larmor frequency and is given by $\phi_L = \gamma\omega T_E$. The pulse sequence shown in Fig. 14 consists of interleaved CPMG sequences at different frequencies. We now analyze the spin dynamics for this sequence and show that it is possible to compensate for the B-S effects by slight modifications of the phase and timing of the excitation pulses.

Between two refocusing pulses, the total phase shift for a spin in a slice consists of the standard Larmor phase shift ϕ_L, plus $N_s - 1$ B–S phase shifts induced by the $N_s - 1$ refocusing pulses on the other slices. For the CPMG sequence on the first slice, the phase shift between the excitation pulse and its first refocusing pulse remains half the total phase shift. This is the case because the B–S shift is proportional to the pulse duration and it is assumed that the refocusing pulses are twice as long and of the same amplitude as the excitation pulses. For the CPMG sequence on the second slice, this equality is not fulfilled any more: Between the excitation pulse and the first refocusing pulse on slice 2, the RF pulse on slice 1 is a 180 degree pulse and the associated B–S phase shift is twice as long as desired. Therefore, the total phase shift before the first refocusing pulse is increased by:

$$\Delta\phi_{BS,2} = -\left(\frac{\pi}{4}\right)\frac{\omega_1}{\Delta\omega_0}. \tag{14}$$

For the third slice, we get extra phase shifts from the first and second slice. It is easy to generalize this effect for the k-th slice, where we get $k - 1$ contributions:

$$\Delta\phi_{BS,k} = -\left(\frac{\pi}{4}\right)\frac{\omega_1}{\Delta\omega_0}\left(1+\frac{1}{2}+\frac{1}{3}+\ldots\frac{1}{k-1}\right). \tag{15}$$

We can account for this phase shift by replacing the $(\pi/2)_x$ excitation pulse for slice k by a phase-shifted excitation pulse $(\pi/2) - \Delta\phi_{BS,k}$.

In this analysis, we have implicitly assumed that the B-S phase shift is constant within a slice. Eq. (13) shows that this is not exactly the case because the offset frequency $\Delta\omega$ varies linearly across the slice. This dependence can also be compensated for (to first order) by shifting the position of the excitation pulse for the k-th slice slightly:

$$\delta\tau_k = \frac{t_\pi}{2}\left[1+\frac{1}{2^2}+\frac{1}{3^2}+\ldots\frac{1}{(k-1)^2}\right]. \tag{16}$$

Another example where the RF frequency varies from pulse to pulse is in spin-echo sequences modified to measure the average magnitude of B_1 [24–26]. These sequences rely upon measuring the B–S phase shift intentionally produced by RF pulses that are far-off resonance. A narrow band system would not allow the transmission of far off-resonance pulses to observe this effect. We have modified the BS-CPMG sequence described in [26] to use constant-amplitude, non-selective RF pulses for this purpose. The sequence consists of a normal CPMG pulse train, but with additional off-resonant pulses of length T_{BS} applied after every refocusing pulse. Two variants are shown in Fig. 15. The spin dynamics of both sequences are identical, except for a reversal in the sign of the B–S phase shift ϕ_{BS}. However, the latter is preferable for smaller echo spacings because it provides more time for the receiver to recover after RF pulses.

As before, we denote the offset frequency of the off-resonant pulses by $\Delta\omega$ and assume that they are far off-resonance, i.e., $|\Delta\omega| \gg \omega_1$. The B–S shift caused by these pulses will vary across the excited slice, as shown in (13), resulting in distorted echo shapes. This dependence can be removed to first order by taking the difference between two scans with offset frequencies of $\Delta\omega$ and $-\Delta\omega$, resulting in

$$\phi_{BS}(\Delta\omega) - \phi_{BS}(-\Delta\omega) \approx T_{BS}\left(\frac{\omega_1^2}{\Delta\omega}\right). \tag{17}$$

This result is quite insensitive to the flip angle of the CPMG pulses, which is fortunate since, if ω_1 is uncertain, so will be the flip angles. Thus (17) can be directly used to estimate ω_1. However, in practice the off-resonant pulses excite small but often non-negligible amounts of transverse magnetization, which produce amplitude variations in the final echo and make it difficult to measure ϕ_{BS} precisely. This effect is particularly pronounced for rectangular pulses, which have poor frequency selectivity. We can eliminate such unwanted magnetization by phase cycling the off-resonant pulses. In addition, unless T_{BS} is an integer multiple of $1/(\Delta\omega)$, the rotating frames of the off-resonant and CPMG pulses will not be aligned after each off-resonant pulse, resulting in an additional static phase offset of the echoes. This offset can be estimated and removed by running scans for two or more values of T_{BS}.

Fig. 15 shows experimentally measured B-S shifts using the CPMG-BS2 sequence on a doped water sample. The estimated

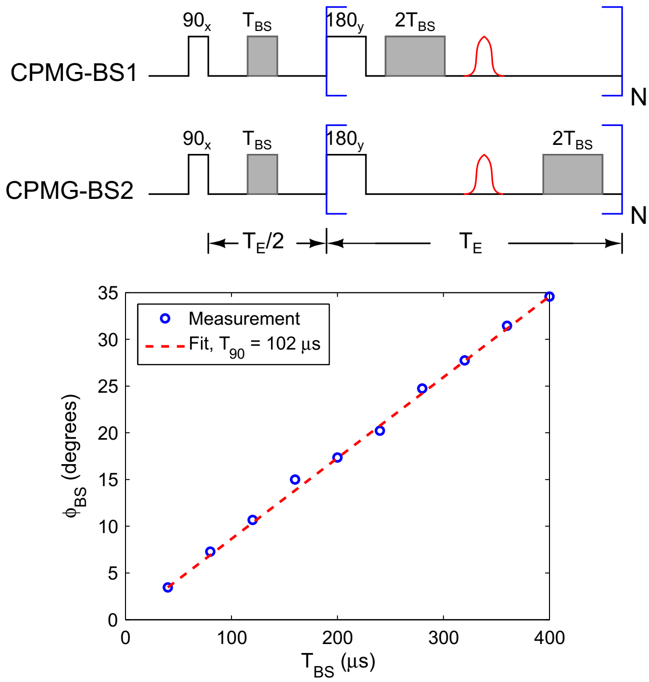

Fig. 15. Modified CPMG pulse sequence for measuring Bloch–Siegert shifts (top), and experimental results (bottom). Off-resonant pulses used to induce the shift are shown in gray shading, while nominally on-resonant pulses are unshaded. Echoes are shown in red. The sample for the experiment was NiCl solution ($T_2 = 110$ ms). Other experimental parameters include $f_0 = 1.48$ MHz, $T_E = 2.4$ ms, and $\Delta f_{RF} = 25$ kHz. (For interpretation of the references to color in this figure legend, the reader is referred to the web version of this article.)

value of $\omega_1 = \pi/(2T_{90})$ matches that obtained from other measurements.

3.3. Chemical identification: NQR

Our broadband MR system could also be useful for nuclear quadruple resonance (NQR), particularly ^{14}N NQR. NQR signals can be observed without an external magnetic field, making it an excellent technique for field detection of chemicals, e.g. explosives, narcotics, and pharmaceuticals. Pulsed NQR of ^{14}N has been studied extensively for its characteristics as a fingerprint for identification of explosives [7,27] and contaminated drugs [28]. Each nitrogen atom in a molecule generates three NQR lines, because the ^{14}N nucleus, which has spin $I = 1$, exhibits three energy levels in the presence of an electric field gradient. These resonant frequencies, which are often denoted by ω_+, ω_-, and $\omega_0 = \omega_+ - \omega_-$, span a broad range (approximately 0.1–6 MHz for ^{14}N) and are temperature-sensitive. As a result, it is difficult to build a tuned system that detects a variety of samples. This problem disappears if we use our broadband MR system, which allows us to easily switch the RF frequency between and during pulse sequences.

A spin-locked spin echo (SLSE) pulse sequence is commonly used for pulsed NQR experiments. The SLSE sequence consists of a single excitation pulse followed by a series of spin-echo sandwiches. The excitation pulse is phase-shifted by $\pi/2$ with respect to the refocusing pulses, and the flip angle of all the pulses is typically fixed at β. The maximum signal for powder samples is obtained when $\beta = 0.66 \times \pi$. The SLSE sequence causes spin locking in the average B_1 field generated by the train of RF pulses. The resultant echo decay is often bi-exponential, with fast-decaying and slow-decaying components. Experimentally, it is found that the time constant T_{SLSE} of the slowly-decaying component increases as the echo spacing T_E decreases, and approaches $T_{1\rho} \gg T_2$ as $T_E \to 0$. This property makes the SLSE sequence useful for generating a large number of echoes that can be added together to improve SNR.

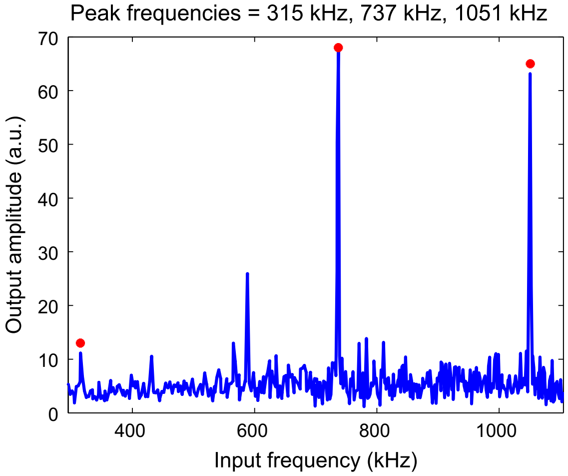

Fig. 16. A broadband scan of the full NQR spectrum of glycine, which has a single nitrogen site with three resonances: $\omega_+/(2\pi) \approx 1052$ kHz, $\omega_-/(2\pi) \approx 737$ kHz, and $\omega_0/(2\pi) \approx 315$ kHz (all marked by dots). The other peaks are due to external RF interference. The experiment was performed on 22.9 gm of glycine powder. The spectrum was built up by adding together $N_E = 80$ echoes produced by an SLSE pulse sequence, averaging across $N_{avg} = 256$ scans, and then incrementing the RF frequency by $\Delta f = 10$ kHz.

Fig. 16 shows that we can measure the full NQR spectrum of glycine (spanning the range 0.3–1.1 MHz) without any hardware tuning. Detecting multiple NQR transitions in this manner can improve the rate of positive identification of chemicals and reduce false alarms. We have also successfully performed ^{14}N and ^{39}K NQR measurements on a variety of other common compounds in solid powder form, such as sodium nitrite, proline, potassium nitrate, and paracetamol (a common analgesic also known as acetaminophen).

4. Conclusion

In this paper we have described a extremely broadband system for low-frequency MR. Our probe design addresses the challenges of low-field NMR and NQR, such as low SNR, inhomogeneous magnetic fields, and limited bandwidth of tuned probes, by avoiding the use of resonant analog circuits. We have shown that this approach provides several advantages for experiments in the 0.1–3 MHz frequency range, such as programmability, flexibility, and robustness. Another benefit of our approach is ease of use. By making the front-end electronics extremely broadband we allow the user to focus on the resonances and dynamics of the spin system, rather than that of the electronics. These advantages may further expand field applications of MR, such as well-logging, rock core analysis, and detection of illicit substances such as explosives and drugs.

We have used our system to perform a wide variety of MR experiments, some of which have been briefly described in the text. More detailed discussions of these experiments will be provided in later publications. Extension to higher frequencies is possible at least for small coils (such as micro coils with low inductance [29]) given recent developments in semiconductor devices. For example, the wide availability of low-noise transistors constructed from high-mobility compound semiconductors such as SiGe may make it possible to increase the bandwidth of the receiver and lower its noise figure. Similarly, improved high-power and high-speed FETs constructed from materials such as GaN and SiC may allow us to increase the power-handling capability and operating frequency range of the transmitter.

Acknowledgments

We thank David McCowan and James Haug at Schlumberger-Doll Research for their help with assembly of the electronics and probe boxes. We also thank Marc Thompson for several useful discussions.

References

[1] E. Fukushima, S.B.W. Roeder, Experimental Pulse NMR: A Nuts and Bolts Approach, first ed., Westview Press, Boulder, CO, 1981.

[2] T. Hopper, S. Mandal, D. Cory, M. Hürlimann, Y.-Q. Song, Low-frequency NMR with a non-resonant circuit, J. Magn. Reson. 210 (1) (2011) 69–74.

[3] S. Mandal, S. Utsuzawa, Y.-Q. Song, An extremely broadband low-frequency MR system, Micropor. Mesopor. Mater. 178 (2013) 5355.

[4] B. Hills, Applications of low-field NMR to food science, Ann. Rep. NMR Spectrosc. 58 (2006) 177–230.

[5] F. Casanova, J. Perlo, B. Blümich (Eds.), Single-Sided NMR, Springer, 2011.

[6] M.D. Hürlimann, Well logging, in: Encyclopedia of Magnetic Resonance, John Wiley & Sons, New York, 2012.

[7] J. Miller, G. Barrall, Explosives detection with nuclear quadrupole resonance, Am. Sci. 93 (1) (2005) 50–57.

[8] E. Schempp, P.J. Bray, Nuclear quadrupole resonance spectroscopy, in: D. Henderson (Ed.), Physical Chemistry, An Advanced Treatise, vol. IV, Academic Press, 1970, pp. 521–632.

[9] T.M. Brill, S. Ryu, R. Gaylor, J. Jundt, D.D. Griffin, Y.-Q. Song, P.N. Sen, M.D. Hürlimann, Nonresonant multiple spin echoes, Science 297 (5580) (2002) 369–372.

[10] D.I. Hoult, G. Kolansky, D. Kripiakevich, A 'Hi-Fi' cartesian feedback spectrometer for precise quantitation and superior performance, J. Magn. Reson. 171 (2004) 57–63.

[11] I.J. Lowe, M. Engelsberg, A fast recovery pulsed nuclear magnetic resonance sample probe using a delay line, Rev. Sci. Inst. 45 (5) (1974) 631–639.

[12] I.J. Lowe, D.W. Whitson, Homogeneous RF field delay line probe for pulsed nuclear magnetic resonance, Rev. Sci. Inst. 48 (3) (1977) 268–274.

[13] A. Kubo, S. Ichikawa, Ultra-broadband NMR probe: numerical and experimental study of transmission line NMR probe, J. Magn. Reson. 162 (2) (2003) 284–299.

[14] D. Murphree, S. Cahn, D. Rahmlow, D. DeMille, An easily constructed, tuning free, ultra-broadband probe for NMR, J. Magn. Reson. 188 (1) (2007) 160–167.

[15] D.I. Hoult, R.E. Richards, The signal-to-noise ratio of the nuclear magnetic resonance experiment, J. Magn. Reson. 24 (1976) 71–85.

[16] D.I. Hoult, Receiver design for MR, eMagRes, 2011, pp. 1–21.

[17] D.I. Hoult, Fast recovery high sensitivity NMR probe and preamplifier for low frequencies, Rev. Sci. Inst. 50 (2) (1979) 193–200.

[18] G. Gonzalez, Microwave Transistor Amplifiers: Analysis and Design, second ed., Prentice Hall, 1996.

[19] S. Utsuzawa, S. Mandal, Y.-Q. Song, Transformer-coupled NMR probe, J. Magn. Reson. 216 (0) (2012) 128–133.

[20] M.D. Hürlimann, Carr–Purcell sequences with composite pulses, J. Magn. Reson. 152 (2001) 109–123 (15).

[21] V.D.M. Koroleva, S. Mandal, Y.Q. Song, M.D. Hürlimann, Broadband CPMG sequence with short composite refocusing pulses, J. Magn. Reson. 230 (2013) 64–75.

[22] S. Mandal, V.D.M. Koroleva, T.W. Borneman, Y.-Q. Song, M.D. Hürlimann, Axis-matching excitation pulses for CPMG-like sequences in inhomogeneous fields, J. Magn. Reson. 237 (2013) 1–10.

[23] F. Bloch, A. Siegert, Magnetic resonance for nonrotating fields, Phys. Rev. 57 (6) (1940) 522–527.

[24] L.I. Sacolick, F. Wiesinger, I. Hancu, M.W. Vogel, B_1 mapping by Bloch–Siegert shift, Magn. Reson. Med. 63 (5) (2010) 1315–1322.

[25] L.I. Sacolick, L. Sun, M.W. Vogel, W.T. Dixon, I. Hancu, Fast radiofrequency flip angle calibration by Bloch–Siegert shift, Magn. Reson. Med. 66 (5) (2011) 1333–1338.

[26] T.C. Basse-Lüsebrink, V.J.F. Sturm, T. Kampf, G. Stoll, P.M. Jakob, Fast CPMG-based Bloch–Siegert B_1^+ mapping, Magn. Reson. Med. 67 (2) (2011) 405–418.

[27] J. Fraissard, O. Lapina (Eds.), Explosives Detection using Magnetic and Nuclear Resonance Techniques, Springer, 2009.

[28] E. Balchin, D.J. Malcolme-Lawes, I.J.F. Poplett, M.D. Rowe, J.A.S. Smith, G.E.S. Pearce, S.A.C. Wren, Potential of nuclear quadrupole resonance in pharmaceutical analysis, Anal. Chem. 77 (13) (2005) 3925–3930.

[29] A.G. Webb, Radiofrequency microcoils for magnetic resonance imaging and spectroscopy, J. Magn. Reson. (2012) 1–12.